Technical Article

Non-conforming Finite Elements

Abstract— **We investigate flexible discretization techniques for the approximate solution of electromagnetic field problems. In order to keep as much flexibility as possible, we use independently generated grids which are well suited for approximating the solution of decoupled local sub-problems in each subdomain, coupled on a common interface. Therefore, we have to deal with the situation of non-conforming grids appearing at the common interface of two subdomains. Special care has to be taken in order to define and implement the appropriate discrete coupling operators. The Finite Element method is applied and used in two approaches to handle non-conforming grids: (1) Classical mortaring and (2) Nitsche-type mortaring. The first approach guarantees a strong coupling of the flux by introducing a Lagrange multiplier and a weak coupling of the magnetic vector potential. The Nitsche-type mortaring does not need the additional Lagrange multiplier and handles the coupling by symmetrizing the bilinear form, as well as adding a special interface term to penalize the jump of the magnetic vector potential.**

The first part of this contribution descibes step by step the FE formulations of both non-conforming grid techniques and its application to two 2D examples: solenoid and gear wheel sensor. The second part focuses on the correct Nitsche-type mortaring formulation for 3D electromagnetics and its application to induction heating. Thereby, the application of a multi-harmonic ansatz (harmonic balance finite element method) allows to solve the nonlinear electromagnetic field problem in the frequency domain.

I. INTRODUCTION

In many technical applications a device is immersed in an acoustic fluid, e.g. ultrasound transducers for non-destructive testing as well as medical diagnostic and therapy, capacitive microphones, electrodynamic loudspeakers, noise radiated by power transformers (see, e.g. [1]). Furthermore, the numerical simulation of the actuator mechanism within the structure is quite complex, since in most cases we have to deal with a nonlinear coupled problem (e.g. the magnetic-mechanical as well as electrostatic-mechanical principle), where in addition to the nonlinear coupling terms each single field is nonlinear (e.g., geometric nonlinearity in mechanics, nonlinear or even hysteretic modeling of ferromagnetic materials, moving body problem in the electromagnetic field) [1]. Furtheron, in most cases the discretization within the structure has to be much finer than the one we need for the acoustic wave propagation in the fluid. For standard Finite-Element (FE) methods computational meshes are required to be conforming. This means that either uniform grids which result in many unknowns (c.f. Fig. 1) or many transition elements between fine subdomain grids and coarse ones (c.f. Fig. 2) need to be applied to maintain high quality and accuracy of the result. This is the only possible choice, if the standard conforming FE method is used, since it can only handle a geometrically conforming triangulation. Unfortunately, the accuracy of the numerical solution depends very sensitively on the shape regularity of the underlying mesh.

Thus, a small transition zone from fine to coarse meshes results in a poor numerical approximation. Therefore, in order to meet the requirements of different mesh sizes and to
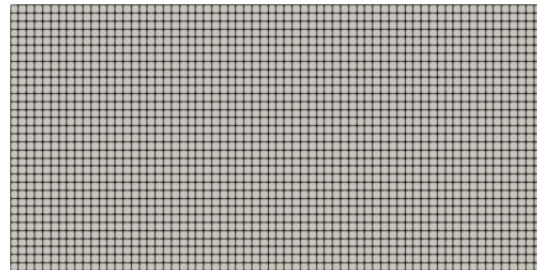
Fig. 1: Uniform
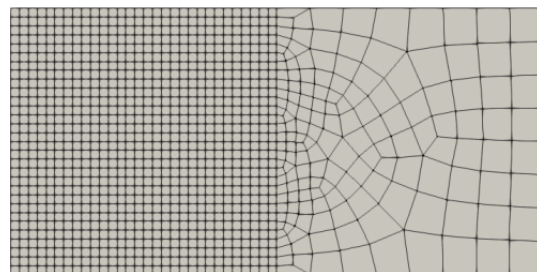
Fig. 2: Coarsening
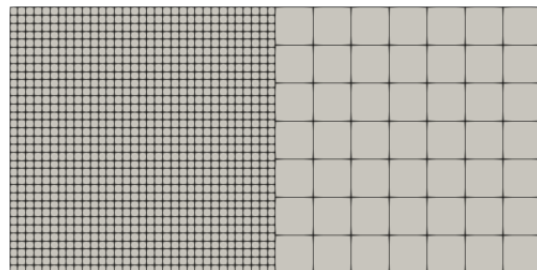
Fig. 3: Non-conforming

gain full flexibility for the discretization, we propose to use a non-conforming FE method (c.f. Fig. 3). The advantages of this method can be summarized as follows:

- Pre-processing is much more flexible and therefore efficient, since mesh generations in the different subdomains do not influence each other.

- The approximation order can be chosen independently for each subdomain. This permits to use higher order elements in regions, where the solution is known to be smooth and fine discretizations using low order elements may be used in regions, where singularities in the solution occur.

- The method can be used for parallelization. If only a single physical field is involved, our method can be classified as a FE Tearing and Interconnection dual-primal (FETI-DP) method in domain decomposition terms, see, e.g. [2], [3].

Generally speaking, non-conforming methods deal with solving the transmission problem [4], i.e., transferring a physical field from one side of the non-conforming interface to the other side. A straight forward approach is to perform a strong point-wise coupling in the sense of nodal values using a two- or three-field hybrid method, see, e.g. [5]. In the two-field method, the primary unknowns and the Lagrange multipliers (constraining the primary unknowns) along the interface between the master and the slave side are considered as field variables. In the three-field methods, a further unknown, having the properties of the primary unknown, is introduced as an additional field variable. The main drawback of these approaches is that just a suboptimal convergence behavior is achieved (see, e.g. [6]). Being precise, it means that in the H^1-norm, which measures both the error of the unknown and of the first order spatial derivative (corresponding to the physical flux), is only of order $O(h^{1/2})$ with h as a characteristic discretization size. Within the context of structural mechanics, these methods of the master-slave concept have been combined with the uniform strain approach [7] to improve the convergence rate, especially for the computation of the mechanical stresses. Such a method passes the patch test but still shows oscillations of the mechanical stress between a minimum and a maximum value, which is invariant under mesh refinement [6], [7]. Therefore, further effort was necessary and resulted in the framework of Mortar FE formulations. Here, additional degrees of freedom along the non-conforming interface in form of Lagrange multipliers, now being the flux of the primary unknown, are introduced and the strong continuity of the solution across the interface is replaced by a weak one. Originally introduced for coupling of spectral and finite element methods [8], the analysis of Mortar methods has been extended to three-dimensional problems (see, e.g. [9]) and hp-finite elements (see, e.g. [10]). The introduction of dual Lagrange multipliers in [11] allowed to locally eliminate the Lagrange multipliers. Towards 3D electromagnetics, care has to be taken to achieve appropriate Lagrange multipliers. Mortar edge element methods with emphasis on the proper construction of Lagrange multiplier spaces along the skeleton of the decomposition as well as on the effcient solution of the resulting discrete saddle point problem can be found in [12], [13]. Still a major challenge within Mortar methods is the quality of the intersection mesh needed to evaluate the coupling integrals, e.g.

$$\int_{\Gamma_I} N_{1i} \, N_{2j} \, \mathrm{d}\boldsymbol{s} \,,$$

where along the common non-conforming interface Γ_I N_{ni} is the ith basis function from side n. Since the two involved basis functions are defined on different meshes (slave and master side), the evaluation of the integral is not trivial, and is even more involved, when curved interfaces are present (for details see, e.g. [1]). A FE mesh is typically created by means of an optimization strategy. The purpose of the optimization algorithm is to maximize the element quality under the given constraints (max. distortion ratio, element size, ...). The intersection mesh is generated under the

constraint of the two adjacent surface meshes. Consider the coplanar interface in Fig. 4a. Every vertex of either surface mesh has to be contained in the intersection mesh. For slightly mismatching meshes (see magnification), this results in high aspect-ratio elements, high-lighted in Fig. 4b. To avoid high aspect-ratio elements, one may discard them

(a) Surface meshes.

(b) Intersection mesh.
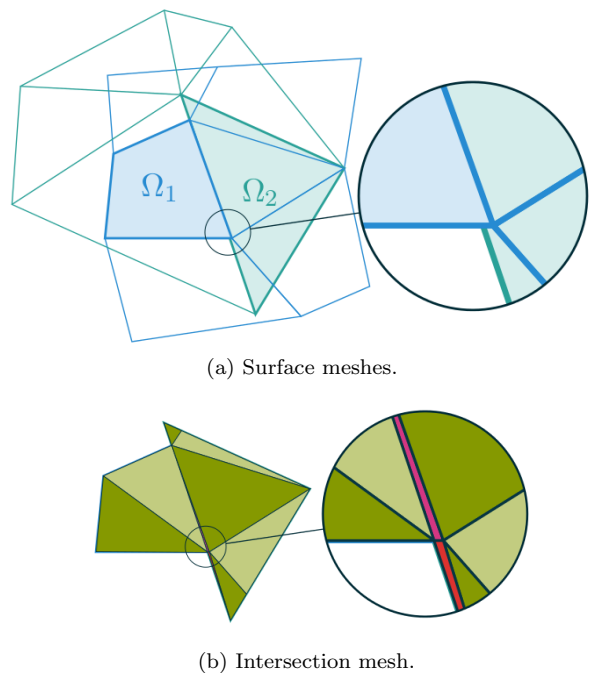
Fig. 4: Coplanar interface with the two surface meshes from Ω_1 and Ω_2 and the resulting intersection mesh.

or allow slight overlaps. These mesh irregularities may cause numerical oscillations for the Mortar method [14]. Therefore, further efforts to improve non-conforming mesh techniques have been undertaken and resulted in so-called Nitsche-type mortaring. The method of Nitsche [15] was originally introduced to weakly impose essential boundary conditions. This idea has been applied in [16] in the context of non-conforming meshes for the classical Laplace equation. Thereby, optimal a priori error estimates in both the energy norm and the L_2 norm for polynomials of arbitrary degree (but the same at both sides) have been achieved. The robustness of this approach has been strongly improved in [17] for the cases of intersection elements with small volume fractions and large material heterogeneities.

Within the last years, we have further improved non-conforming mesh techniques and applied it to many different coupled field problems: vibro-acoustics [18], [19], electro-thermal coupling [20], incompressible free-surface flow [21] and aeroacoustics [22], [23].

The rest of the paper is structured as follows. In Sec. II we describe step by step the FE formulations of both non-conforming mesh techniques and its application to two 2D examples: solenoid and gear wheel sensor. Next, Sec. III discusses the FE formulation and important detailsype mortaring for 3D electromagnetics using edge finite elements. The application of Nitsche-type mortaring to 3D electromagnetics is demonstarted in Sec. IV for induction heating. Thereby, the use of a multi-harmonic

ansatz (harmonic balance finite element method) allows to solve the nonlinear electromagnetic field problem in the frequency domain. Finally, we provide a conclusion and an outlook for further for computer implementation of Nitsche-t research.

II. FORMULATIONS

We consider Maxwell's equation for the magnetostatic case. For the 2D plane case (xy-plane is assumed), the partial differential equation (PDE) for the magnetic vector potential reads as

$$-\nabla \nu(\boldsymbol{x})\nabla u = J_{\mathrm{z}} \quad \text{in} \quad \Omega, \tag{1}$$
$$u = u_{\mathrm{e}} \quad \text{on} \quad \Gamma. \tag{2}$$

Thereby, u is the z-component of the magnetic vector potential $\boldsymbol{A} = (0,0,u)^{\top}$, ν the magnetic reluctivity and J_{z} the z-component of the current density.
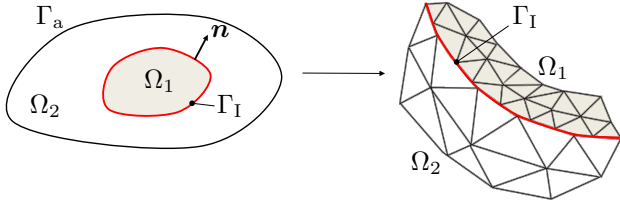
Fig. 5: Computational domain with two subregions Ω_1 and Ω_2 with different discretizations.

A. Classical Mortar

In order to reformulate (1) on the decomposed domain with possibly discontinuous functions on the skeleton (see Fig. 5), weak coupling conditions have to be introduced within the Mortar framework. In a strong sense, the jump $[u] = u_1 - u_2$ of the subdomain functions across the inner interfaces is zero

$$[u] = 0 \text{ on } \Gamma_{\mathrm{I}}.$$

This condition has to be reformulated as a weak condition using test functions μ from a suitable Lagrange multiplier space M (see [11], [6])

$$\int_{\Gamma_{\mathrm{I}}} [u] \, \mu \, \mathrm{d}\boldsymbol{s} = 0 \quad \forall \, \mu \in M \quad \text{and} \quad [\mathrm{u}] \, \in \mathrm{H}^{1/2}(\Gamma_{\mathrm{I}}).$$

Furthermore, it is also postulated that the flux of the unknown is continuous across the interfaces Γ_{I} in normal direction. The condition on the jump of the normal derivatives is therefore $[\nu \partial u/\partial \boldsymbol{n}] = 0$, where $\boldsymbol{n}$ is defined with respect to the outward pointing slave side. This can be achieved by introducing a Lagrange multiplier

$$\lambda = -\nu_s \frac{\partial u_s}{\partial \boldsymbol{n}} = -\nu_m \frac{\partial u_m}{\partial \boldsymbol{n}} \circ \Phi \text{ on } \Gamma_{\mathrm{I}}. \tag{3}$$

Here Φ denotes a spatial mapping, which relates the points on the slave sides to the points on the master sides of the interfaces. The weak formulation of the Laplace problem can now be rewritten by substituting the definition of the

Lagrange multiplier according to (3). The arising boundary integral over the outer boundary is set to zero for simplicity. Summing up, one arrives at the symmetric saddle point problem for two subdomains as displayed in Fig. 5: Finding (u_i, λ) and $i = 1, 2$ such that

$$\sum_{i=1}^{2} \left(\int_{\Omega_i} \nu_i(\boldsymbol{x})\nabla u_i \cdot \nabla v_i \, \mathrm{d}\boldsymbol{x} - \int_{\Omega_i} J_{\mathrm{zi}}\nabla v \, \mathrm{d}\boldsymbol{x} \right)$$
$$+ \int_{\Gamma_{\mathrm{I}}} [v] \, \lambda \, \mathrm{d}\boldsymbol{s} = 0$$
$$\int_{\Gamma_{\mathrm{I}}} [u] \, \mu \, \mathrm{d}\boldsymbol{s} = 0 \tag{4}$$

for all (μ, v_i). It shall be noted that μ is a test function with the same basis as the Lagrange multiplier λ. This property is responsible for the symmetry of the arising stiffness matrix.

A spatial discretization by standard finite elements results in the following algebraic system of equations

$$\begin{pmatrix} \boldsymbol{K}_{11} & 0 & \boldsymbol{D} \\ 0 & \boldsymbol{K}_{22} & \boldsymbol{M} \\ \boldsymbol{D}^{\top} & \boldsymbol{M}^{\top} & 0 \end{pmatrix} \begin{pmatrix} \underline{u_1} \\ \underline{u_2} \\ \underline{\lambda} \end{pmatrix} = \begin{pmatrix} \underline{f_1} \\ \underline{f_2} \\ \underline{0} \end{pmatrix}. \tag{5}$$

In (5) $\boldsymbol{K}_{11}, \boldsymbol{K}_{22}$ are standard stiffness matrices of the subdomains. The matrices $\boldsymbol{D}$ and $\boldsymbol{M}$ are due to the non-conforming interface and are formally mass-like matrices. They compute element-wise, with $\bigwedge$ as the assembly operator,

$$\boldsymbol{D} = \bigwedge_{e=1}^{n_{\mathrm{es}}} \boldsymbol{d}^e, \, \boldsymbol{d}^e = [d_{ab}],$$
$$d_{ab} = \int_{\Gamma_e} N_a^s N_b^s \, \mathrm{d}\boldsymbol{s}, \tag{6}$$
$$\boldsymbol{M} = \bigwedge_{e=1}^{n_{\mathrm{isec}}} \boldsymbol{m}^e, \, \boldsymbol{m}^e = [m_{ab}],$$
$$m_{ab} = \int_{\Gamma_e} (N_a^m \circ F_m^{-1} \circ \Phi)(N_b^s \circ F_s^{-1}) \, \mathrm{d}\boldsymbol{s}. \tag{7}$$

Here n_{es} is the number of surface elements on the slave side of the interface and n_{isec} is the number of intersection elements on the interface. The finite element basis functions N_a^s and N_a^m denote the traces of the FE basis on the slave and on the master side of the interface, N_b^s denotes the Lagrange multiplier basis given with respect to the slave side and F^{-1} is the mapping from element global to local coordinates. The necessary steps for the computation of the integrals in (7) are discussed in Sec. II-C.

B. Nitsche-Type Mortaring

The method of Nitsche [15] was originally introduced to impose essential boundary conditions weakly. Unlike the penalty method, it is consistent with the original differential equation. The benefit of Nitsche's method is that it retains the convergence rate of the underlying FE method, whereas the standard penalty method either requires a very large penalty parameter or massively increases the condition number of the resulting algebraic system of equations.

We apply Nitsche's ansatz for a computational domain consisting of two subdomains Ω_1 and Ω_2 with a common interface Γ_I as displayed in Fig. 5. We introduce two test functions v_1 and v_2 and write the weak formulation of each subdomain individually

$$\int_{\Omega_1} \nu_1 \, \nabla v_1 \cdot \nabla u_1 \mathrm{d} \, \mathrm{d}\boldsymbol{x} \quad - \quad \int_{\Gamma_I} \nu_1 \, v_1 \frac{\partial u_1}{\partial \boldsymbol{n}_1} \, \mathrm{d}\boldsymbol{s}$$
$$= \int_{\Omega_1} v_1 J_{z1} \, \mathrm{d}\boldsymbol{x} \qquad (8)$$

$$\int_{\Omega_2} \nu_2 \, \nabla v_2 \cdot \nabla u_2 \, \mathrm{d}\boldsymbol{x} \quad - \quad \int_{\Gamma_I} \nu_2 \, v_2 \frac{\partial u_2}{\partial \boldsymbol{n}_2} \, \mathrm{d}\boldsymbol{s}$$
$$= \int_{\Omega_2} v_2 J_{z2} \, \mathrm{d}\boldsymbol{x} \,. \qquad (9)$$

For the sake of a simpler notation, we choose ν_1 and ν_2 constant in Ω_1 and Ω_2, which is by no means a restriction. In general, the material parameter can even depend on the physical quantity u. In a next step, we add the two equations (8) and (9), introduce a common normal direction $\boldsymbol{n} = \boldsymbol{n}_1 = -\boldsymbol{n}_2$, and thus use

$$\nu_1 \frac{\partial u_1}{\partial \boldsymbol{n}_1} \quad = \quad \nu_1 \frac{\partial u_1}{\partial \boldsymbol{n}} = \nu_2 \frac{\partial u_2}{\partial \boldsymbol{n}_2} = -\nu_2 \frac{\partial u_2}{\partial \boldsymbol{n}}$$

to arrive at

$$\int_{\Omega_1} \nu_1 \, \nabla v_1 \cdot \nabla u_1 \, \mathrm{d}\boldsymbol{x} + \int_{\Omega_2} \nu_2 \, \nabla v_2 \cdot \nabla u_2 \, \mathrm{d}\boldsymbol{x}$$
$$- \int_{\Gamma_I} \nu_1 \, [v] \frac{\partial u_1}{\partial \boldsymbol{n}} \, \mathrm{d}\boldsymbol{s} = \int_{\Omega_1} v_1 J_{z1} \, \mathrm{d}\boldsymbol{x} + \int_{\Omega_2} v_2 J_{z2} \, \mathrm{d}\boldsymbol{x} \,.$$

In order to retain symmetry, we add the term

$$- \int_{\Gamma_I} \nu_1 \frac{\partial v_1}{\partial \boldsymbol{n}} \, [u] \, \mathrm{d}\boldsymbol{s} \quad \text{with} \quad [u] = u_1 - u_2 \,.$$

This operation is allowed, since we postulate on the interface $u_1 = u_2$. In a final step, we add the penalization term

$$\beta \bar{\nu} \sum_{E(\Gamma_I)} \frac{p_E^2}{h_E} \int_{\Gamma_E} [v] \, [u] \, \mathrm{d}\boldsymbol{s}$$

with β a penalty factor, p_E the polynomial degree of the FE basis function, h_E the characteristic element size, and $\bar{\nu}$ the averaged reluctivity given by $(\nu_1 + \nu_2)/2$. Therewith,

we arrive at the final formulation for Nitsche's approach

$$\int_{\Omega_1} \nu_1 \, \nabla v_1 \cdot \nabla u_1 \, \mathrm{d}\boldsymbol{x} + \int_{\Omega_2} \nu_2 \, \nabla v_2 \cdot \nabla u_2 \, \mathrm{d}\boldsymbol{x}$$
$$- \underbrace{\int_{\Gamma_I} \nu_1 \, [v] \frac{\partial u_1}{\partial \boldsymbol{n}} \, \mathrm{d}\boldsymbol{s}}_{\text{Consistency}} - \underbrace{\int_{\Gamma_I} \nu_1 \, \frac{\partial v_1}{\partial \boldsymbol{n}} \, [u] \, \mathrm{d}\boldsymbol{s}}_{\text{Symmetrization}}$$
$$+ \underbrace{\beta \bar{\nu} \sum_{E(\Gamma_I)} \frac{p_E^2}{h_E} \int_{\Gamma_E} [v] \, [u] \, \mathrm{d}\boldsymbol{s}}_{\text{Penalty/Stabilization}}$$
$$= \int_{\Omega_1} v_1 J_{z1} \, \mathrm{d}\boldsymbol{x} + \int_{\Omega_2} v_2 J_{z2} \, \mathrm{d}\boldsymbol{x} \,. \qquad (10)$$

If the penalty parameter β in (10) is chosen large enough, the bilinear form is coercive on the discrete space $V_h \subset H^1$ and one can derive optimal a priori error estimates in both the energy norm and the L_2 norm for polynomials of arbitrary degree [16].

As in the case of classical Mortar formulation, we will also need all operations (projection of coordinates, intersection operations, etc.) between the two surface meshes in order to compute the entries of the matrices. Now, the matrix system of equations reads as follows

$$\begin{pmatrix} \boldsymbol{K}_{11} & 0 \\ 0 & \boldsymbol{K}_{22} \end{pmatrix} \begin{pmatrix} \underline{u}_1 \\ \underline{u}_2 \end{pmatrix}$$
$$+ \begin{pmatrix} \boldsymbol{K}_{\Gamma_1} & \boldsymbol{K}_{\Gamma_1 \Gamma_2} \\ \boldsymbol{K}_{\Gamma_2 \Gamma_1} & \boldsymbol{K}_{\Gamma_2} \end{pmatrix} \begin{pmatrix} \underline{u}_1 \\ \underline{u}_2 \end{pmatrix} = \begin{pmatrix} \underline{f}_1 \\ \underline{f}_2 \end{pmatrix} \,. \qquad (11)$$

Here, $\boldsymbol{K}_{11}$, $\boldsymbol{K}_{22}$ are the standard stiffness matrices of the individual subdomains. The entries of the additional matrices compute as

$$\boldsymbol{K}_{\Gamma_1}^{ij} = - \int_{\Gamma_1} \nu_1 \, N_{1i} \frac{\partial N_{1j}}{\partial \boldsymbol{n}} \, \mathrm{d}\boldsymbol{s} - \int_{\Gamma_1} \nu_1 \frac{\partial N_{1i}}{\partial \boldsymbol{n}} \, N_{1j} \, \mathrm{d}\boldsymbol{s}$$
$$+ \beta \bar{\nu} \sum_{E(\Gamma_1)} \frac{p_E^2}{h_E} \int_{\Gamma_E} N_{1i} N_{1j} \, \mathrm{d}\boldsymbol{s}$$

$$\boldsymbol{K}_{\Gamma_1 \Gamma_2}^{ij} = \int_{\Gamma_1} \nu_1 \frac{\partial N_{1i}}{\partial \boldsymbol{n}} \, N_{2j} \, \mathrm{d}\boldsymbol{s}$$
$$- \beta \bar{\nu} \sum_{E(\Gamma_1)} \frac{p_E^2}{h_E} \int_{\Gamma_E} N_{1i} N_{2j} \, \mathrm{d}\boldsymbol{s} \qquad (12)$$

$$\boldsymbol{K}_{\Gamma_2 \Gamma_1}^{ij} = \int_{\Gamma_1} \nu_1 \, N_{2i} \frac{\partial N_{1j}}{\partial \boldsymbol{n}} \, \mathrm{d}\boldsymbol{s}$$
$$- \beta \bar{\nu} \sum_{E(\Gamma_1)} \frac{p_E^2}{h_E} \int_{\Gamma_E} N_{2i} N_{1j} \, \mathrm{d}\boldsymbol{s}$$

$$\boldsymbol{K}_{\Gamma_2}^{ij} = \beta \bar{\nu} \sum_{E(\Gamma_2)} \frac{p_E^2}{h_E} \int_{\Gamma_E} N_{2i} N_{2j} \, \mathrm{d}\boldsymbol{s} \,.$$

Here, we have already substituted Γ_I by Γ_1 as well as Γ_2, which are the discretized interfaces (see Fig. 6). Note that
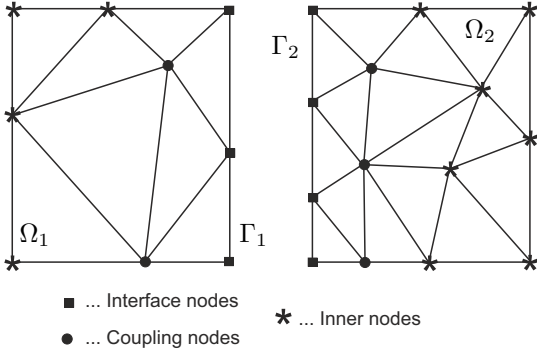
Fig. 6: Discretized subdomains Ω_1 and Ω_2.

- ■ ... Interface nodes
- ● ... Coupling nodes
- ✶ ... Inner nodes

Fig. 7: Four possible cases of two lines intersecting each other.

not only nodes on the interfaces but also neighboring nodes in Ω_1 and in Ω_2 are involved, since the computation of some entries require normal derivatives. Studying the structure of our coupled system of equations, the formulation is symmetric and does not introduce any additional unknowns (we have no Lagrange multiplier as in case of Mortar FEM). However, a penalty parameter β, must be chosen large enough to guarantee $u_1 = u_2$ but not too large to deteriorate the condition number of the system matrix.

Finally, we want to note that Nitsche-type mortaring is equivalent to an IP-DG (Internal Penalty - Discontinuous Galerkin) ansatz along the non-conforming interface Γ_I.

C. Intersection Operations and Computation of Coupling Matrices

To demonstarte the principle approach, we consider intersections of line elements in 2D. If the interface is planar this amounts to perform simple interval checks. If the interface is curved, the elements have to be projected onto a common line segment prior to the interval checks.

If an intersection of two co-linear line elements exists, it is again a line element sharing two of the four endpoints of both parent elements in the co-linear case. To check for an intersection one has to project the endpoints $[\boldsymbol{m}_1, \boldsymbol{m}_2]$ of the element on the master side of the interface in two dimensional coordinates to the one dimensional local coordinate system defined by the endpoints of the slave element $[\boldsymbol{s}_1, \boldsymbol{s}_2]$.

The local coordinates of the slave nodes $[\mathbf{s_1}, \mathbf{s_2}]$ are trivially given by 0 and 1. The four local coordinates of the pair of lines are then brought into ascending order and therefore four possible cases for the intersection of two line elements may be identified (see Fig. 7):

1. $\xi_1 < 0 \wedge 0 < \xi_2 \leq 1$: the intersection is the line $[\boldsymbol{s}_1, \boldsymbol{m}_2]$

2. $0 \leq \xi_1 < 1 \wedge \xi_2 > 1$: the intersection is the line $[\boldsymbol{m}_1, \boldsymbol{s}_2]$

3. $\xi_1 \leq 0 \wedge \xi_2 \geq 1$: the intersection is the line $[\boldsymbol{s}_1, \boldsymbol{s}_2]$

4. $\xi_1 > 0 \wedge \xi_2 < 1$: the intersection is the line $[\boldsymbol{m}_1, \boldsymbol{m}_2]$

The intersection calculation on curved interfaces is more complicated since the elements have to be mapped to a common plane before the actual intersection calculation can be performed. A possible approach, proposed in [6] relies on pair-wise mappings of the elements to the plane or line
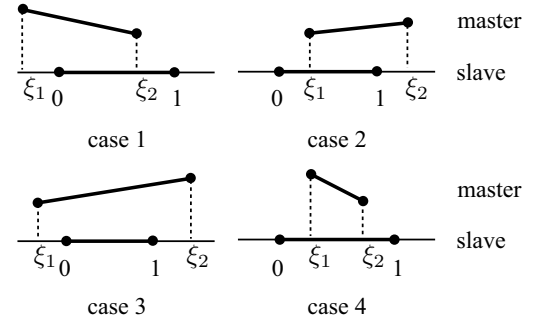
of the element on the slave side of the interface along the face normal vector.

Once the intersection elements have been found, the coupling integrals (7) and (12) can be evaluated by means of standard Gauss quadrature. For a single element the integral can be rewritten as follows

$$
\int_{\Gamma_e} (N_a^m \circ F_m^{-1} \circ \Phi)(N_b^s \circ F_s^{-1}) \, \mathrm{d}\boldsymbol{s} \approx
$$
$$
\sum_{l=1}^{n_{\mathrm{int}}} W_l N_a(\boldsymbol{\xi}_l^m) N_b(\boldsymbol{\xi}_l^s) \mathcal{J}_{F_e}(\boldsymbol{\xi}_l^e) \, . \tag{13}
$$

Here n_{int} is the number of integration points, W_l are the integration weights and the determinant of the Jacobian $\mathcal{J}^e$ accounts for the change in volume due to the element mapping. By using this integration formula the difficulty arises that only the integration point $\boldsymbol{\xi}_l^e$ with respect to the local coordinates of the intersection element is known in advance and that the points $\boldsymbol{\xi}_l^m$ in the master element and $\boldsymbol{\xi}_l^s$ in the slave element have to be projected before the basis functions can be evaluated (see Fig. 8).

- ● Element nodes
- ■ Integration points
- □ Nodes of intersec. element
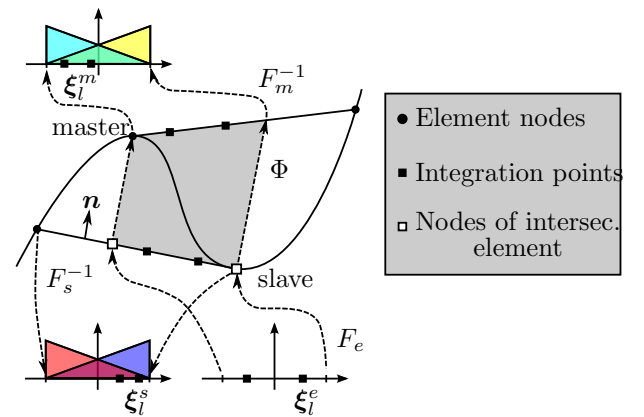
Fig. 8: Projection of integration points from the intersection element into the master element which is of first order and into the slave element which is of second order in this example.

It is very important to notice that nodes of the intersection element do not carry any degrees of freedom by themselves. The intersection element is just an auxiliary geometrical entity which only serves as integration domain. The

projection operation for general elements involves the following steps [25]:

1. Map local coordinates $\boldsymbol{\xi}_l^e$ of integration point in intersection element to global coordinates using F_e.

2. Project global coordinates of integration point on slave side to global coordinate on master side using Φ.

3. Map global coordinates of integration point to local coordinates $\boldsymbol{\xi}_l^m$ of master element using F_m^{-1}.

4. Map global coordinates of integration point to local coordinates $\boldsymbol{\xi}_l^s$ of slave element using F_s^{-1}.

Points 3 and 4 in general involve the application of a Newton-Raphson algorithm. A linear mapping algorithm may only be used for 2-node isoparametric line elements, 3-node isoparametric triangle elements or higher order elements which just use a linear local-to-global mapping. Once the values of the basis functions N_a and N_b have been obtained and (13) has been evaluated, the assembly operator adds the contribution to the corresponding entry in the coupling matrix.

For further details concerning intersection operations, especially in the 3D case, see [25]. In addition, we want to mention the idea of a virtual coupling interface on which the degrees of freedom are defined globally with respect to the geometry and represented by means of basis splines. The interface geometry is given by non-uniform rational basis splines (nurbs), or generalized basis splines, allowing for an exact description of curved interfaces, an aspect incorporated from isogeometric analysis [14], [26].

D. Computational Results

In order to investigate the different approaches, we consider in a first case a solenoid as displayed in Fig. 9. Here, we have generated three different meshes: (1)
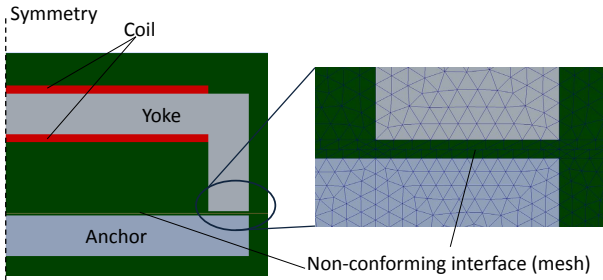
Fig. 9: Computational setup of the solenoid and detail of non-conforming mesh with the non-conforming interface just in the air region.

a conforming mesh for reference computations; (2) a non-conforming mesh, where the interface is completely inside the air region (see Fig. 9); (3) a non-conforming mesh, where the interface includes a part of the surface of the yoke (see Fig. 10). For the iron core (yoke and anchor), we consider a nonlinear BH-curve and perform computations on the conforming mesh as well as the two non-conforming meshes. Figure 11 shows the resulting magnetic flux density.
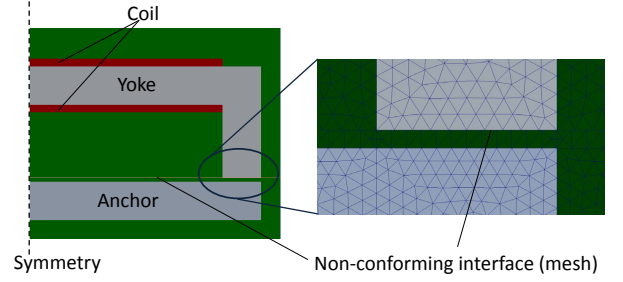
Fig. 10: Computational setup of the solenoid and detail of non-conforming mesh with the non-conforming interface including the iron core.

Comparing the computed fields, no visible differences can be seen, and so Fig. 11 just displays the results obtained by the classical Mortar approach. To perform a more detailed
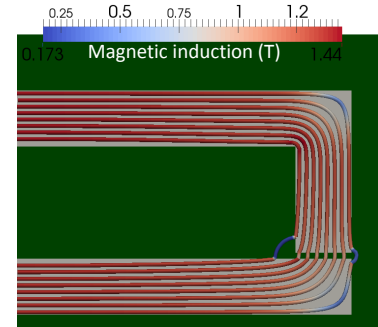
Fig. 11: Computed magnetic flux lines in case of non-conforming mesh using Mortar formulation.

analysis, we compute the magnetic energy in the yoke and the anchor region. Table I lists the results obtained by the conforming mesh as well as non-conforming mesh according to Fig. 9. We have also investigated in different penalty factors β for the Nitsche-type mortaring method. As it can be seen, in case of $\beta = 500$ we obtain the smallest error compared to computations with the conforming mesh. In conclusion, we can state that the Nitsche-type mortaring approach is quite robust w.r.t. the penalty factor β and can be even superior to the classical Mortar method if the optimal value for β is chosen. These findings also hold in the case, where the non-conforming interface is not completely in air but also contains a part of the surface of the yoke, where the magnetic reluctivity is discontinuous (see Tab. II).

In a second case study, we consider a gear wheel sensor as displayed in Fig. 12, consisting of a permanent magnet, a coil, and the gear wheel. Since the wheel is rotating and the sensor is fixed, we just have to use a fine mesh in the vicinity of the sensor. As can be seen in Fig. 12, the other regions have a quite coarse mesh. Here, we have to treat curved interfaces, when applying the methods for non-conforming meshes. Details of the mesh are displayed in Fig. 13. In a first investigation, we have filled the air gaps of the gear wheel also with iron, so that instead of the gear-wheel we have an iron cylinder. When rotating the iron cylinder, we should obtain no changes in the magnetic flux detected

TABLE I: Magnetic energy in Ws (computations with classical Mortar and Nitsche-type mortaring on the non-conforming mesh according to Fig. 9)

	Conform (Ws)	Mortar (Ws)	Error
Anchor	5288.62	5348.27	1.13 %
Yoke	8268.42	8372.63	1.26 %

	Nitsche $\beta = 20$ (Ws)	Error	Nitsche $\beta = 100$ (Ws)	Error
Anchor	5347.38	1.11 %	5329.47	0.77 %
Yoke	8371.11	1.24 %	8339.55	0.86 %

	Nitsche $\beta = 500$ (Ws)	Error	Nitsche $\beta = 1000$ (Ws)	Error
Anchor	5275.94	0.24 %	5233.28	1.05 %
Yoke	8243.98	0.30 %	8167.48	1.22 %

TABLE II: Magnetic energy in Ws (computations with classical Mortar and Nitsche-type mortaring on the non-conforming mesh according to Fig. 10).

	Conform (Ws)	Mortar (Ws)	Error
Anchor	5288.62	5347.8	1.12 %
Yoke	8268.42	8371.03	1.24 %

	Nitsche $\beta = 20$ (Ws)	Error	Nitsche $\beta = 100$ (Ws)	Error
Anchor	5360.19	1.35 %	5340.34	0.97 %
Yoke	8393.31	1.50 %	8356.8	1.07 %

	Nitsche $\beta = 500$ (Ws)	Error	Nitsche $\beta = 1000$ (Ws)	Error
Anchor	5303.95	0.29 %	5274.77	0.26 %
Yoke	8288.53	0.24 %	8233.72	0.42 %

Fig. 12: Computational setup and mesh of the gear wheel with sensor.

Fig. 13: Detail of non-conforming mesh.

by the sensor. Thereby, any change in the computed flux has to be caused by the numerical scheme. Applying the classical Mortar as well as Nitsche-type mortaring and computing the flux for a rotation of 60 rpm, we obtain a constant flux for all positions of the iron sphere. This clearly demonstrates the robustness of both methods and our implementation of the intersection operations on curved interfaces.

In a second investigation, we rotate the gear-wheel at 60 rpm, apply both non-conforming formulations and compute the magnetic fields. Figure 14 displays the magnetic flux lines at a certain position of the gear-wheel w.r.t. the sensor. One can observe smooth flux lines over the non-conforming interface without any perturbations. Furthermore, the computed flux is displayed in Fig. 15 and shows no numerical disturbances. This example strongly demonstrates the advantages of the non-conforming methods. One can perform the geometric modeling and meshing individually for all subdomains and then glue them together by classical Mortar or Nitsche-type mortaring. Furthermore, in case of rotating systems, e.g., in electrical drives, gear-wheel sensors, etc. we do not need any re-meshing and interpolation, which often introduces strong numerical errors.

III. Nitsche-type mortaring for 3D electromagnetics

In this section, we will derive a non-conforming Nitsche-type mortaring for the eddy current problem, using the magnetic vector potential formulation. For very low frequency applications, there is also the possibility to introduce a scalar potential on the interface, as proposed in [26], in order to scale the gradient and rotational components differently.

A. Nitsche Method for the Eddy Current Case

We want to solve the general (static $\kappa = 0$, transient $\kappa = \gamma \, \partial / \partial t$, harmonic $\kappa = j\omega\gamma$) eddy current problem on the domain Ω: Find $\boldsymbol{A} \in V := \{\boldsymbol{A}' \in H(\mathrm{curl}) : \mathrm{tr}_\tau \boldsymbol{A}' = 0 \text{ on } \Gamma_D\}$ such that

$$\int_\Omega \nabla \times \boldsymbol{A} \cdot \nu \nabla \times \boldsymbol{A}' \, \mathrm{d}\boldsymbol{x} + \int_\Omega \kappa \boldsymbol{A} \cdot \boldsymbol{A}' \, \mathrm{d}\boldsymbol{x} = \int_\Omega \boldsymbol{J} \cdot \boldsymbol{A}' \, \mathrm{d}\boldsymbol{x},$$

$$\forall \boldsymbol{A}' \in V, \quad (14)$$

where Γ_D is the Dirichlet boundary. For non conducting regions, we apply a regularization with a small artificial
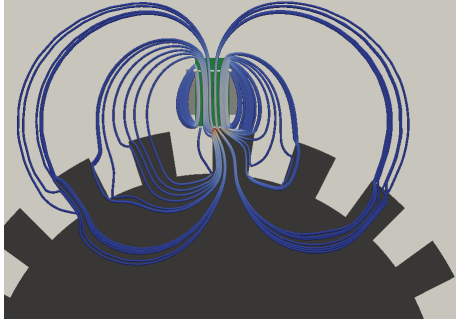
Fig. 14: Magnetic flux lines.
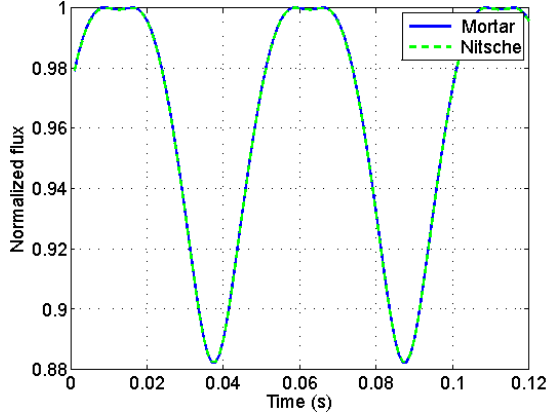
Fig. 15: Magnetic flux change detected by the measurement coil for 60rpm.

conductivity γ' and it can be shown that the solution $\boldsymbol{A}_{\gamma'}$ converges to the real solution $\boldsymbol{A}$ for $\gamma' \to 0$.

For Nitsche-type mortaring, we assume two domains Ω_1 and Ω_2, as depicted in Fig. 5, with outer boundaries Γ_1, Γ_2 and the common interface region Γ_{I}. The eddy current problem for the two domains reads as

$$\int_{\Omega_1} \left(\nabla \times \boldsymbol{A}_1 \cdot \nu_1 \nabla \times \boldsymbol{A}_1' + \kappa \boldsymbol{A}_1 \cdot \boldsymbol{A}_1' \right) \mathrm{d}\boldsymbol{x} -$$
$$\underbrace{\int_{\Gamma_1} (\nu_1 \, \nabla \times \boldsymbol{A}_1 \times \boldsymbol{n}) \cdot \boldsymbol{A}_1' \, \mathrm{d}\boldsymbol{s}}_{\text{standard BC}} -$$
$$\int_{\Gamma_{\mathrm{I}}} (\nu_1 \, \nabla \times \boldsymbol{A}_1 \times \boldsymbol{n}) \cdot \boldsymbol{A}_1' \, \mathrm{d}\boldsymbol{s} = \int_{\Omega_1} \boldsymbol{J}_1 \cdot \boldsymbol{A}_1' \, \mathrm{d}\boldsymbol{x} \qquad (15)$$

$$\int_{\Omega_2} \left(\nabla \times \boldsymbol{A}_2 \cdot \nu_2 \nabla \times \boldsymbol{A}_2' + \kappa \boldsymbol{A}_2 \cdot \boldsymbol{A}_2' \right) \mathrm{d}\boldsymbol{x} -$$
$$\underbrace{\int_{\Gamma_2} (\nu_2 \, \nabla \times \boldsymbol{A}_2 \times \boldsymbol{n}) \cdot \boldsymbol{A}_2' \, \mathrm{d}\boldsymbol{s}}_{\text{standard BC}} -$$
$$\int_{\Gamma_{\mathrm{I}}} (\nu_2 \, \nabla \times \boldsymbol{A}_2 \times \boldsymbol{n}) \cdot \boldsymbol{A}_2' \, \mathrm{d}\boldsymbol{s} = \int_{\Omega_2} \boldsymbol{J}_2 \cdot \boldsymbol{A}_2' \, \mathrm{d}\boldsymbol{x}. \qquad (16)$$

The standard BC will be neglected in the following. We are not restricted to write the surface terms in the above form. We can use the following vector identities:

$$(\nabla \times \boldsymbol{A} \times \boldsymbol{n}) \cdot \boldsymbol{A}' \equiv (\boldsymbol{n} \times \boldsymbol{A}') \cdot \nabla \times \boldsymbol{A} \equiv$$
$$(\boldsymbol{A}' \times \nabla \times \boldsymbol{A}) \times \boldsymbol{n}. \qquad (17)$$

At this point, let us review the interface conditions

$$\boldsymbol{A}_1 \times \boldsymbol{n}_1 = -\boldsymbol{A}_2 \times \boldsymbol{n}_2, \qquad (18)$$

$$\nu_1 \nabla \times \boldsymbol{A}_1 \times \boldsymbol{n}_1 = -\nu_2 \nabla \times \boldsymbol{A}_2 \times \boldsymbol{n}_2, \qquad (19)$$

where $\boldsymbol{n}_1, \boldsymbol{n}_2$ are the outward pointing normal vectors at the common interface Γ_{I} of the two subdomains.

Depending on the formulation we choose in (17), we use the first or the second interface condition and add (15) and (16)

$$\sum_{i=1}^{2} \left(\int_{\Omega_i} \left(\nabla \times \boldsymbol{A}_i \cdot \nu_i \nabla \times \boldsymbol{A}_i' + \kappa \boldsymbol{A}_i \cdot \boldsymbol{A}_i' \right) \mathrm{d}\boldsymbol{x} \right) -$$
$$\int_{\Gamma_{\mathrm{I}}} \left((\nu_1 \, \nabla \times \boldsymbol{A}_1 \times \boldsymbol{n}) \cdot \boldsymbol{A}_1' - (\nu_1 \, \nabla \times \boldsymbol{A}_1 \times \boldsymbol{n}) \cdot \boldsymbol{A}_2' \right) \mathrm{d}\boldsymbol{s} =$$
$$\sum_{i=1}^{2} \left(\int_{\Omega_i} \boldsymbol{J}_i \cdot \boldsymbol{A}_i' \, \mathrm{d}\boldsymbol{x} \right), \qquad (20)$$

where we have implicitly used $\boldsymbol{n} = \boldsymbol{n}_1 = -\boldsymbol{n}_2$. Applying the jump operator $[\boldsymbol{u}] = \boldsymbol{u}_1 - \boldsymbol{u}_2$, for a certain field quantity $\boldsymbol{u}$, we can compactly write

$$\sum_{i=1}^{2} \left(\int_{\Omega_i} \left(\nabla \times \boldsymbol{A}_i \cdot \nu_i \nabla \times \boldsymbol{A}_i' + \kappa \boldsymbol{A}_i \cdot \boldsymbol{A}_i' \right) \mathrm{d}\boldsymbol{x} \right) -$$
$$\int_{\Gamma_{\mathrm{I}}} (\nu_1 \, \nabla \times \boldsymbol{A}_1 \times \boldsymbol{n}) \cdot [\boldsymbol{A}'] \, \mathrm{d}\boldsymbol{s} = \sum_{i=1}^{2} \left(\int_{\Omega_i} \boldsymbol{J}_i \cdot \boldsymbol{A}_i' \, \mathrm{d}\boldsymbol{x} \right). \qquad (21)$$

To obtain the Nitsche-type mortaring formulation, we follow the steps discussed in Sec. II-B and add in a first stept the penalty term

$$\beta \overline{\nu} \int_{\Gamma_{\mathrm{I}}} \frac{p_E^2}{h_E} [\boldsymbol{A} \times \boldsymbol{n}] \cdot [\boldsymbol{A}' \times \boldsymbol{n}] \, \mathrm{d}\boldsymbol{s}. \qquad (22)$$

The second step is to add a symmetrization term to ensure that the resulting system is symmetric. Thereby, we arrive at the following form

$$\sum_{i=1}^{2} \left(\int_{\Omega_i} \left(\nabla \times \boldsymbol{A}_i \cdot \nu_i \nabla \times \boldsymbol{A}_i' + \kappa \boldsymbol{A}_i \cdot \boldsymbol{A}_i' \right) \mathrm{d}\boldsymbol{x} \right) -$$
$$\underbrace{\int_{\Gamma_{\mathrm{I}}} (\nu_1 \, \nabla \times \boldsymbol{A}_1 \times \boldsymbol{n}) \cdot [\boldsymbol{A}'] \, \mathrm{d}\boldsymbol{s}}_{\text{Consistency}} -$$
$$\underbrace{\int_{\Gamma_{\mathrm{I}}} (\nu_1 \, \nabla \times \boldsymbol{A}_1' \times \boldsymbol{n}) \cdot [\boldsymbol{A}] \, \mathrm{d}\boldsymbol{s}}_{\text{Symmetrization}}$$
$$+ \underbrace{\beta \overline{\nu} \int_{\Gamma_{\mathrm{I}}} \frac{p_E^2}{h_E} [\boldsymbol{A} \times \boldsymbol{n}] \cdot [\boldsymbol{A}' \times \boldsymbol{n}] \, \mathrm{d}\boldsymbol{s}}_{\text{Penalty}} = \sum_{i=1}^{2} \left(\int_{\Omega_i} \boldsymbol{J}_i \cdot \boldsymbol{A}_i' \, \mathrm{d}\boldsymbol{x} \right). \qquad (23)$$

An important aspect when implementing this method is to apply the correct transformation of vector quantities (magnetic vector potential) to the reference element and back. Therefore, the next section is dedicated to this issue.

B. Surface Integration and Transformation of Vector Quantities

When using FE methods, it is essential to think about the transformation from the parametric- (reference-) element to the physical element via so called *Piola* transforms or to be more precise *Piola-like* transforms, as mentioned in [27]. Before we elaborate on this transformations, we first have to define the correct function space, in which the solution is computed. In $H(\text{curl})$, the degrees of freedom are defined using tangential components along edges and in $H(\text{div})$, using normal components over faces [29]. To stay as general as possible, one has to consider the *de-Rham complex* in continuous and discrete form as displayed in Fig. 16 (see, e.g. [29]), where Π denotes the interpolation from the continuous function space to the discrete one.
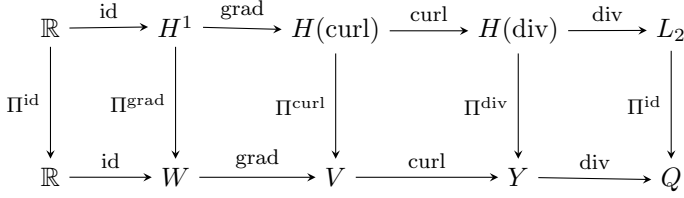
Fig. 16: *De-Rham complex* in continuous and discrete form.

For mapping a scalar or vector from a reference element to the phyical one, one has to define a bijective smooth mapping $\Phi : \hat{\Omega} \to \Omega$, see Fig. 17. This mapping Φ does,
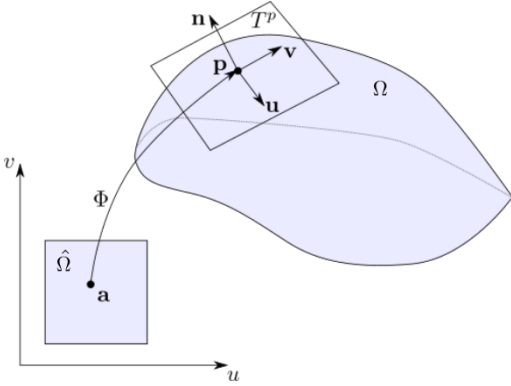
Fig. 17: Non isometric mapping.

in general, not have to be isometric. An *isometric mapping* means that the length-measure in vector space 1 is the same as in the mapped space 2, for example when drawing a line on a piece of paper and bending the paper, the length of the line on the bent sheet is still equal to the non-mapped line length. Since this mapping Φ does not have to be isometric, we need to take care of the different metrics (notion of length) between our two spaces [30]. According to [27], one can distinguish three cases:

- Mapping Cartesian- to Cartesian-coordinates,

- Mapping Curvilinear- to Cartesian-coordinates,

- Mapping Curvilinear- to Curvilinear-coordinates,

from which we will elaborate on the first one (for further details, we refer to [27]).

In the following, the transformation rules for the four different function spaces are presented, as outlined in the de-Rham complex (see Fig. 16) and for the appropriate operator. Therefore, we introduce four quantities and perform the transformations (subspace $\hat{\Omega}$ for the reference domain and Ω for the physical one):

$$w \in \mathbb{R}: \quad \begin{aligned} \boldsymbol{v}_{\hat{\Omega}} &= \tilde{\boldsymbol{J}}^{-\top} \boldsymbol{v}_{\Omega} \circ \Phi^{-1}, \\ \nabla_{\hat{\Omega}} \times \boldsymbol{v}_{\hat{\Omega}} &= |\tilde{\boldsymbol{J}}|^{-1} \tilde{\boldsymbol{J}} \left(\nabla_{\Omega} \times \boldsymbol{v}_{\Omega} \right) \circ \Phi^{-1} \end{aligned}$$

$$\boldsymbol{v} \in H(\text{curl}): \quad \begin{aligned} \boldsymbol{v}_{\hat{\Omega}} &= \tilde{\boldsymbol{J}}^{-\top} \boldsymbol{v}_{\Omega} \circ \Phi^{-1}, \\ \nabla_{\hat{\Omega}} \times \boldsymbol{v}_{\hat{\Omega}} &= |\tilde{\boldsymbol{J}}|^{-1} \tilde{\boldsymbol{J}} \left(\nabla_{\Omega} \times \boldsymbol{v}_{\Omega} \right) \circ \Phi^{-1} \end{aligned}$$

$$\boldsymbol{y} \in H(\text{div}): \quad \begin{aligned} \boldsymbol{y}_{\hat{\Omega}} &= |\tilde{\boldsymbol{J}}|^{-1} \tilde{\boldsymbol{J}} \, \boldsymbol{y}_{\Omega} \circ \Phi^{-1}, \\ \nabla_{\hat{\Omega}} \cdot \boldsymbol{y}_{\hat{\Omega}} &= |\tilde{\boldsymbol{J}}|^{-1} (\nabla_{\Omega} \cdot \boldsymbol{y}_{\Omega}) \circ \Phi^{-1} \end{aligned}$$

$$q \in L_2: \quad q_{\hat{\Omega}} = |\tilde{\boldsymbol{J}}|^{-1} q_{\Omega},$$

where $\tilde{\boldsymbol{J}}$ is the Jacobi matrix. Concluding, the normal and tangential vectors can be transformed via $\boldsymbol{t}_{\hat{\Omega}} = \tilde{\boldsymbol{J}} \, \boldsymbol{t}_{\Omega}$ and $\boldsymbol{n}_{\hat{\Omega}} = |\tilde{\boldsymbol{J}}| \tilde{\boldsymbol{J}}^{-\top} \boldsymbol{n}_{\Omega}$.

C. Implementation Details

In (23), the crucial terms, which have to be handled with great care, are the surface integral terms. In the following, the term providing consistency in (23) is chosen to be a representative for the other two surface terms.

According to Ciarlet [41], a finite element consists of a geometric domain Ω, a local element space V_{Ω} of dimension N_{Ω} and a set of linearly independent functionals $\{\psi_{\Omega,1}, ..., \psi_{\Omega,N_{\Omega}}\}$ on Ω, which are the degrees of freedom. The local functionals can then be identified with global ones to control the continuity of the global space. According to the definition of a finite element from above, we can define the (lowest order) Nédélec finite element on a triangle as

- triangle T

- local space $\boldsymbol{N}_0$, e.g. for a triangle:
  $\boldsymbol{N}_0 := \left\{ v = (a_x, \ a_y)^\top + b(y, \ -x)^\top \right\}$

- the functionals, associated with the edges $E_{\alpha,\beta}$

$$\psi_{E_{\alpha,\beta}} : \mathbf{v} \to \int_{E_{\alpha,\beta}} \mathbf{v} \cdot \tau \, \mathrm{d}\boldsymbol{s}. \tag{24}$$

According to [1], we can now discretize the continuous function-space using edge elements

$$\boldsymbol{A} \approx \sum_{a=1}^{m_{\text{eqns}}} \boldsymbol{N}_a \cdot \psi_{E_{\alpha,\beta}}$$

and obtain

$$\int_{\Gamma_{\text{I}}} (\nu_1 \, \nabla \times \boldsymbol{A}_1 \times \boldsymbol{n}) \cdot [\boldsymbol{A}'] \, \mathrm{d}\boldsymbol{s} \approx$$

$$\sum_{a=1}^{m_{\text{eqns}}} \sum_{b=1}^{m_{\text{eqns}}} \int_{\Gamma_{\text{I}}} (\nu_1 \nabla \times \boldsymbol{N}_a \times \boldsymbol{n}) \cdot [\boldsymbol{N}_b] \, \mathrm{d}\boldsymbol{s} \, \psi_{E_{\alpha,\beta}}. \tag{25}$$

Thereby, we have to keep three issues in mind:

1. H(curl) shape functions: Assume we have a 3D geometry and Γ_I is a surface interface between two regions, meshed in a non-conforming way. We can use 2D reference finite elements or it is also possible to use 3D H(curl) elements and evaluate them at the surface. This is possible because 3D H(curl) basis functions based on [28], degenerate to the corresponding 2D shape functions on a surface.

2. Surface integration: Looking at the jump operator in (25), we have to evaluate the difference of the vector potential, respectively the shape functions between the master and slave surface mesh and integrate over the master surface. In our implementation, this is achieved by projecting in normal direction each point of evaluation from Γ_1 of the corresponding 3D element onto Γ_2 and evaluate there.

3. Transformation to the reference element: The last part is the correct transformation of the surface integrals from global to local coordinates, based on the presented Cartesian to Cartesian mappings.

IV. APPLICATION TO INDUCTION HEATING

When simulating induction heating processes, the solution quantity is the temperature distribution $T(\boldsymbol{x}, t)$. The equation, which has to be solved is the heat conduction (diffusion) equation

$$\frac{\partial(\rho c_m(T)\, T)}{\partial t}(\boldsymbol{x}, t) = \nabla \cdot (\lambda(T)\nabla T(\boldsymbol{x}, t)) + \tilde{Q}(T, \boldsymbol{x}, t), \quad (26)$$

where ρ is the density, c_m the specific heat capacity, λ the conduction coefficient and $\tilde{Q}$ the heat source density.
For induction heating processes, we are mainly interested in the steady state solution $t \to \infty$ and we can simplify the time dependent equation to

$$-\nabla \cdot (\lambda(T)\nabla T(\boldsymbol{x}, t)) = Q(T, \boldsymbol{x}), \quad (27)$$

where Q is the consistent steady state (period average) heat source density (Joule and eddy current losses), which will be derived in the following. These losses compute as

$$Q(t) = \boldsymbol{J} \cdot \boldsymbol{E} \quad (28)$$

and the splitting of the total current density into an impressed and a solenoidal part yields

$$\boldsymbol{J} = \boldsymbol{J}_i + \gamma(\boldsymbol{E}_s + \boldsymbol{v} \times \boldsymbol{B}),$$

ands simplifies to

$$Q = (\boldsymbol{J}_i + \gamma \boldsymbol{E}_s) \cdot \boldsymbol{E}, \quad (29)$$

when assuming $\boldsymbol{v} = 0$. From the definition of the magnetic vector potential, we obtain

$$Q = \gamma \frac{\partial \boldsymbol{A}}{\partial t} \cdot \frac{\partial \boldsymbol{A}}{\partial t} + \boldsymbol{J}_i \cdot \frac{\partial \boldsymbol{A}}{\partial t}. \quad (30)$$

A. Multi-harmonic Ansatz

Let us now revisit (14) for the harmonic case with $\kappa = j\omega\gamma$, because we are only interested in the efficient computation of the quasi steady state solution [35], [36], [37]. Thereby, the $\boldsymbol{A}(\boldsymbol{x}, t)$ is called a *periodic steady state solution* if:

- $\boldsymbol{A}(\boldsymbol{x}, t)$ is periodic with period length τ, so that $\boldsymbol{A}(\boldsymbol{x}, t) = \boldsymbol{A}(\boldsymbol{x}, t + \tau)$,

- $\boldsymbol{A}(\boldsymbol{x}, t)$ satisfies the eddy current problem (14) but not necessarily the initial condition.

Using a Fourier expansion for the magnetic vector-potential $\boldsymbol{A}(\boldsymbol{x}, t)$, we obtain

$$\boldsymbol{A}(\boldsymbol{x}, t) = \Re\left(\sum_{k=0}^{N} \hat{\boldsymbol{A}}_k(\boldsymbol{x}) \cdot e^{jk\omega t}\right) = \sum_{k=-N}^{N} \hat{\boldsymbol{A}}_k(\boldsymbol{x}) \cdot e^{jk\omega t}. \quad (31)$$

Following [31], a similar ansatz expands the (solution dependent) magnetic reluctivity

$$\nu(|\nabla \times \boldsymbol{A}(\boldsymbol{x}, t)|) = \sum_{m=-M}^{M} \hat{\nu}_m(\boldsymbol{x}) \cdot e^{jm\omega t}, \quad (32)$$

with $M \leq N$. Inserting this relation into (14) results in the time-harmonic pendants.

As already mentioned, we are now considering a nonlinear (solution dependent material parameter) problem and cannot investigate different harmonics $k\omega, k \in \mathbb{Z}$ independent of each other as in the linear case, which results in a complicated system involving coupled harmonics. In the context of this section, the reluctivity is assumed to be $\nu = \nu(|\boldsymbol{B}|) = \nu(|\nabla \times \boldsymbol{A}|)$, continuous and the corresponding BH-curve must be strongly monotone. Then, we can use the *Browder-Minty theorem* [38] to show that a solution of the nonlinear problem exists uniquely, as performed in [39].

Now we can start with the construction of the nonlinear system by inserting the Fourier expansions (31) and (32) into the eddy current problem (14)

$$\nabla \times \sum_{m=-M}^{M} \hat{\nu}_m(\boldsymbol{x})e^{jm\omega t} \,\nabla \times \sum_{k=-N}^{N} \hat{\boldsymbol{A}}_k(\boldsymbol{x})e^{jk\omega t} =$$

$$\hat{\boldsymbol{J}}_i(\boldsymbol{x})e^{j\omega t} - j\omega\gamma \sum_{k=-N}^{N} k\hat{\boldsymbol{A}}_k(\boldsymbol{x})e^{jk\omega t}. \quad (33)$$

Multiplying this equation by $e^{-i\omega n t}$ for $n \in [-N, ..., N]$ and integrating over one period $\tau = 2\pi/\omega$, we can rewrite the

system, corresponding to [31] as

$$
\begin{aligned}
&\nabla \times
\begin{bmatrix}
\hat{\nu}_0 & \hat{\nu}_{-1} & \dots & \hat{\nu}_{-M} & & & \\
\hat{\nu}_1 & \hat{\nu}_0 & \hat{\nu}_{-1} & & \ddots & & \\
\vdots & & \hat{\nu}_0 & & & \hat{\nu}_{-M} & \\
\hat{\nu}_M & & & \ddots & & & \vdots \\
& \ddots & & & \hat{\nu}_0 & \hat{\nu}_{-1} \\
& & \hat{\nu}_M & \dots & \hat{\nu}_1 & \hat{\nu}_0
\end{bmatrix}
\begin{bmatrix}
\nabla \times \hat{\boldsymbol{A}}_{-N} \\
\vdots \\
\nabla \times \hat{\boldsymbol{A}}_0 \\
\nabla \times \hat{\boldsymbol{A}}_1 \\
\vdots \\
\nabla \times \hat{\boldsymbol{A}}_N
\end{bmatrix} \\
&+ j\omega\gamma
\begin{bmatrix}
-N & & & & & \\
& \ddots & & & & \\
& & 0 & & & \\
& & & 1 & & \\
& & & & \ddots & \\
& & & & & N
\end{bmatrix}
\begin{bmatrix}
\hat{\boldsymbol{A}}_{-N} \\
\vdots \\
\hat{\boldsymbol{A}}_0 \\
\hat{\boldsymbol{A}}_1 \\
\vdots \\
\hat{\boldsymbol{A}}_N
\end{bmatrix}
=
\begin{bmatrix}
0 \\
\vdots \\
0 \\
\hat{\boldsymbol{J}}_1 \\
\vdots \\
0
\end{bmatrix}
\end{aligned}
\tag{34}
$$

The next step is to use a Galerkin ansatz for the spatial discretization of the vector potential, which results in the following system

$$
\begin{aligned}
&\left(
\begin{bmatrix}
\boldsymbol{K}(\hat{\nu}_0) & \boldsymbol{K}(\hat{\nu}_{-1}) & \dots & \boldsymbol{K}(\hat{\nu}_{-M}) & & \\
\boldsymbol{K}(\hat{\nu}_1) & \boldsymbol{K}(\hat{\nu}_0) & \boldsymbol{K}(\hat{\nu}_{-1}) & & \ddots & \\
\vdots & & \boldsymbol{K}(\hat{\nu}_0) & & & \boldsymbol{K}(\hat{\nu}_{-M}) \\
\boldsymbol{K}(\hat{\nu}_M) & & & \ddots & & \vdots \\
& \ddots & & & \boldsymbol{K}(\hat{\nu}_0) & \boldsymbol{K}(\hat{\nu}_{-1}) \\
& & \boldsymbol{K}(\hat{\nu}_M) & \dots & \boldsymbol{K}(\hat{\nu}_1) & \boldsymbol{K}(\hat{\nu}_0)
\end{bmatrix}\right. \\
&\left.+ j\omega
\begin{bmatrix}
-N\boldsymbol{M} & & & & & \\
& \ddots & & & & \\
& & 0 & & & \\
& & & \boldsymbol{M} & & \\
& & & & \ddots & \\
& & & & & N\boldsymbol{M}
\end{bmatrix}\right)
\begin{bmatrix}
\underline{\hat{A}}_{-N} \\
\vdots \\
\underline{\hat{A}}_0 \\
\underline{\hat{A}}_1 \\
\vdots \\
\underline{\hat{A}}_N
\end{bmatrix}
=
\begin{bmatrix}
0 \\
\vdots \\
0 \\
\hat{Q} \\
\vdots \\
0
\end{bmatrix}, \quad (35)
\end{aligned}
$$

where $\boldsymbol{K}(\nu_k)$ is the stiffness matrix associated to the k-th harmonics of the reluctivity and $\boldsymbol{M}$ the mass matrix, which is the same for all harmonics. The vectors $\underline{\hat{A}}_k$ contain the values of the unknown vector potential for harmonic k and $\hat{Q}$ is the right hand side vector, containing the excitition current in fundamental frequency.

Finally, the global system

$$
\boldsymbol{K}_{\mathrm{s}}(\underline{u}_l) \cdot \underline{u}_l = \underline{f}, \tag{36}
$$

is solved via a damped fixed point scheme, where $\boldsymbol{K}_{\mathrm{s}}$ is the whole system matrix

$$
\boldsymbol{K}_{\mathrm{s}} = \boldsymbol{K}(\hat{\nu}_k) + j\omega k\boldsymbol{M}, \quad \text{for} \quad k \in [-N, N] \subset \mathbb{Z}, \tag{37}
$$

$\underline{u}_l$ the current solution vector (consisting of all harmonic vectors $\underline{\hat{A}}_k$ from above) and the right hand side vector $\underline{f}$. The system matrix $\boldsymbol{K}_{\mathrm{s}}$ is a complex matrix $\boldsymbol{K}_{\mathrm{s}} \in \mathbb{C}^{N_h \cdot P \times N_h \cdot P}$, with $P = 2N + 1$ and N_h as the number of spatial dof's. Each submatrix of the overall system matrix is a complex, symmetric matrix. The residual of the current iteration l can be expressed as

$$
\underline{r}_l = \underline{f} - \boldsymbol{K}_{\mathrm{s}}(\underline{u}_l) \cdot \underline{u}_l = \boldsymbol{K}_{\mathrm{s}}(\underline{u}_l) \cdot \underline{d}_l, \tag{38}
$$

where $\underline{d}_l$ is the current deflection vector. By introducing a damping factor $\zeta \in [0, 1] \subset \mathbb{R}$, we can write the new (improved) solution vector as

$$
\underline{u}_{l+1} = \underline{u}_l + \zeta\underline{d}_l = \underline{u}_l + \zeta\boldsymbol{K}_{\mathrm{s}}^{-1}(\underline{u}_l)\left(\underline{f} - \boldsymbol{K}_{\mathrm{s}}(\underline{u}_l) \cdot \underline{u}_l\right). \tag{39}
$$

The first iteration is carried out with $\underline{u}_0$ as the solution of the linear eddy-current problem. Furthermore, the *linear system*

$$
\underline{r}_l = \boldsymbol{K}_{\mathrm{s}}(\underline{u}_l) \cdot \underline{d}_l
$$

for the deflection vector $\underline{d}_l$ is solved by a preconditioned Richardson iteration, with iterator i, damping parameter τ and preconditioner matrix $\boldsymbol{C}$ [31]

$$
\underline{d}_l^{i+1} = \underline{d}_l^i + \tau\boldsymbol{C}^{-1}\left(\underline{r}_l - \boldsymbol{K}_{\mathrm{s}}(\underline{u}_l) \cdot \underline{d}_l^i\right). \tag{40}
$$

Thereby, the off-diagonal elements (sub-system matrices) are "small" compared to the diagonal elements, which allows for a block-Jacobi preconditioner. Now, every diagonal sub-block (sub-matrix) $\boldsymbol{K}_{\mathrm{s},ii}$ for $i = 1, ..., P$ must be inverted

$$
\boldsymbol{C}_k^{-1} = \left(\boldsymbol{K}(\hat{\nu}_0) + j\omega k\boldsymbol{M}\right)^{-1}, \quad \text{for} \quad k \in [-N, N] \subset \mathbb{Z}. \tag{41}
$$

This can efficiently be done by using an algebraic multigrid (AMG) as a preconditioner for a GMRES iteration [32], [33], [34].

At this point it should be noted that the real part of the sub-matrices $\boldsymbol{C}_k$ remains the same for all harmonics ($\boldsymbol{K}(\hat{\nu}_0)$), only the k in the imaginary part changes. Another fact to decrease the storage requirements is, that the off-diagonal elements (sub-matrices) are

$$
\boldsymbol{K}(\pm\hat{\nu}_k) = \boldsymbol{A} \pm j\boldsymbol{B}, \quad \text{with} \quad \boldsymbol{A}, \boldsymbol{B} \in \mathbb{R}^{N_h \times N_h}. \tag{42}
$$

Another aspect, which improves performance massively is the assumption of an excitation in only one harmonic. By doing this, we can cancel out all even rows and columns in the global system matrix and decrease the size of the system to $\boldsymbol{K}_{\mathrm{s}} \in \mathbb{C}^{N_h \cdot P \times N_h \cdot P}$, with $P = N+1$ instead of $P = 2N+1$ from above.

B. Electromagnetic thermal coupling

The Joule and eddy current losses, as defined in (30), are the heat sources

$$
Q = \underbrace{\gamma\frac{\partial \boldsymbol{A}}{\partial t} \cdot \frac{\partial \boldsymbol{A}}{\partial t}}_{\text{Term 1}} + \underbrace{\boldsymbol{J}_i \cdot \frac{\partial \boldsymbol{A}}{\partial t}}_{\text{Term 2}}. \tag{43}
$$

For a better readability, we handle both terms independently.

Term1:. We transform the term from time to frequency domain by applying the multi-harmonic ansatz

$$
\gamma\frac{\partial \boldsymbol{A}}{\partial t} \cdot \frac{\partial \boldsymbol{A}}{\partial t} \rightarrow \gamma\left(\sum_{k=-N}^{N} jk\omega\hat{\boldsymbol{A}}_k e^{jk\omega t} \cdot \sum_{l=-N}^{N} jl\omega\hat{\boldsymbol{A}}_l e^{jl\omega t}\right). \tag{44}
$$

The aim is to integrate all periodic "AC components" (alternating) parts over one period, which then vanish and only the total offset "DC component" (mean value) remains.

Let us now integrate (44) over one period of the base harmonic $\tau_{i+1} - \tau_i = 2\pi/\omega$ and concatenate the double sum

$$\gamma \frac{1}{\tau_{i+1} - \tau_i} \int_{\tau_i}^{\tau_{i+1}} \frac{\partial \boldsymbol{A}}{\partial t} \cdot \frac{\partial \boldsymbol{A}}{\partial t} \, \mathrm{d}t =$$

$$\gamma \omega^2 \frac{-1}{\tau_{i+1} - \tau_i} \int_{\tau_i}^{\tau_{i+1}} \left(\sum_{k=-N}^{N} \sum_{l=-N}^{N} k \, l \, \hat{\boldsymbol{A}}_k \cdot \hat{\boldsymbol{A}}_l e^{j(k+l)\omega t} \right) \mathrm{d}t. \tag{45}$$

At this point we can use the fact that $\int_{\tau_i}^{\tau_{i+1}} e^{jh\omega t} = 0, \forall h \in \mathbb{N}$, which means that all combinations $\hat{\boldsymbol{A}}_k \cdot \hat{\boldsymbol{A}}_l e^{j(k+l)\omega t}$ vanish iff $k + l \neq 0$. Based on this property, we can evaluate the remaining parts (for $k = -l$) as

$$\gamma \frac{1}{\tau_{i+1} - \tau_i} \int_{\tau_i}^{\tau_{i+1}} \frac{\partial \boldsymbol{A}}{\partial t} \cdot \frac{\partial \boldsymbol{A}}{\partial t} \, \mathrm{d}t = \frac{1}{2} \gamma \omega^2 \sum_{k=-N}^{N} k^2 \hat{\boldsymbol{A}}_k \cdot \hat{\boldsymbol{A}}_{-k} =$$

$$\frac{1}{2} \gamma \omega^2 \sum_{k=-N}^{N} k^2 \hat{\boldsymbol{A}}_k \cdot \hat{\boldsymbol{A}}_k^* = \frac{1}{2} \gamma \omega^2 \sum_{k=-N}^{N} k^2 |\hat{\boldsymbol{A}}_k|^2, \tag{46}$$

where $*$ denotes the conjugate complex and $|\cdot|$ the Euclidian norm in $\mathbb{R}^d$. The additional factor of $1/2$ is valid, because in comparison to (45), where the combination $k = -l$ occurs exactly N-times, it occurs $2N$-times in (46).

Based on the above derivation, we obtain the following expression for the first term, where the tilde represents the period averaged quantity

$$\tilde{Q}_{\text{Term 1}} = \frac{1}{2} \gamma \omega^2 \sum_{k=-N}^{N} k^2 \hat{\boldsymbol{A}}_k \cdot \hat{\boldsymbol{A}}_k^* = \frac{1}{2} \gamma \omega^2 \sum_{k=-N}^{N} k^2 |\hat{\boldsymbol{A}}_k|^2 \tag{47}$$

Term2:. For this term, we need to apply the multi-harmonic ansatz for the magnetic vector potential $\boldsymbol{A}(t, \boldsymbol{x}) = \sum_{k=-N}^{N} \hat{\boldsymbol{A}}_k(\boldsymbol{x}) e^{jk\omega t}$ as well as for the impressed current density $\boldsymbol{J}_i(t, \boldsymbol{x}) = \sum_{l=-N}^{N} \hat{\boldsymbol{J}}_{i,l}(\boldsymbol{x}) e^{jl\omega t}$. The challange of this term is the product of two sums with different quantities, contrary to (45). In the most general form, we may write

$$\boldsymbol{J}_i \cdot \frac{\partial \boldsymbol{A}}{\partial t} \to \sum_{l=-N}^{N} \hat{\boldsymbol{J}}_{i,l}(\boldsymbol{x}) e^{jl\omega t} \cdot j\omega \sum_{k=-N}^{N} \hat{\boldsymbol{A}}_k(\boldsymbol{x}) e^{jk\omega t} \tag{48}$$

To simplify (48), we assume the excitation only in the base harmonic $\boldsymbol{J}_1(t) = \hat{\boldsymbol{J}}_1 e^{j1\omega t}$

$$\boldsymbol{J}_1 \cdot \frac{\partial \boldsymbol{A}}{\partial t} \to \hat{\boldsymbol{J}}_i(\boldsymbol{x}) \cdot j\omega \sum_{k=-N}^{N} \hat{\boldsymbol{A}}_k(\boldsymbol{x}) e^{j(k+1)\omega t}. \tag{49}$$

To split the term into a "DC" and an "AC" component, we use the relation for the harmonic current $\hat{\boldsymbol{J}}_1 = \frac{1}{2}(\hat{\boldsymbol{J}}_1 e^{j1\omega t} + \hat{\boldsymbol{J}}_1^* e^{-j1\omega t})$ and obtain

$$\hat{\boldsymbol{J}}_1(\boldsymbol{x}) \cdot j\omega \sum_{k=-N}^{N} \hat{\boldsymbol{A}}_k(\boldsymbol{x}) e^{j(k+1)\omega t} =$$

$$\frac{1}{4} j\omega \sum_{k=-N}^{N} \left(\hat{\boldsymbol{J}}_1 \hat{\boldsymbol{A}}_k e^{j(1+k)\omega t} - \hat{\boldsymbol{J}}_1 \cdot \hat{\boldsymbol{A}}_k^* e^{j(1-k)\omega t} + \right.$$

$$\left. \hat{\boldsymbol{J}}_1^* \cdot \hat{\boldsymbol{A}}_k e^{j(k-1)\omega t} - \hat{\boldsymbol{A}}_k^* \cdot \hat{\boldsymbol{J}}_i e^{j(-1-k)\omega t} \right). \tag{50}$$

Now, we can integrate over one period and compute the average, where we have to consider that in the integration, only the terms with exponent 0 remain. In our case, let us split up the summation over $k = -1, 0, 1$:

- Case $k = -1$:
$$\frac{1}{\Delta T} \int_0^\tau \cdots \mathrm{d}t = \frac{1}{4} j\omega \left(\hat{\boldsymbol{J}}_1 \cdot \hat{\boldsymbol{A}}_k - \hat{\boldsymbol{J}}_1^* \cdot \hat{\boldsymbol{A}}_k^* \right) \cdot (-1)$$

- Case $k = 0$: all terms vanish

- Case $k = 1$:
$$\frac{1}{\Delta T} \int_0^\tau \cdots \mathrm{d}t = \frac{1}{4} j\omega \left(-\hat{\boldsymbol{J}}_1 \cdot \hat{\boldsymbol{A}}_k^* + \hat{\boldsymbol{J}}_1^* \cdot \hat{\boldsymbol{A}}_k \right) \cdot (1)$$

Summing up these three contributions, we obtain the period-averaged Joule losses for the second term

$$\tilde{Q}_{\text{Term 2}} = \frac{1}{4} j\omega \left(\left(\hat{\boldsymbol{J}}_1 \cdot \hat{\boldsymbol{A}}_{-1} + \hat{\boldsymbol{J}}_1^* \cdot \hat{\boldsymbol{A}}_{-1}^* \right) + \left(-\hat{\boldsymbol{J}}_1 \cdot \hat{\boldsymbol{A}}_1^* + \hat{\boldsymbol{J}}_1^* \cdot \hat{\boldsymbol{A}}_1 \right) \right) \tag{51}$$

C. Numerical simulation

We consider an induction heating process as displayed in Fig. 18, where the two ends of the horseshoe shaped inductor represent the connection to the supply. By driving the coil with an alternating current, eddy currents are induced in the sheet and generate eddy current losses, which are heating up the material. The steel sheet has the dimensions 200mm x 200mm x 1mm, with a constant conductivity of $\gamma = 5.08 \cdot 10^6 \, \text{S/m}$. The considered material nonlinearity is taken into account by its commutation curve, depicted in Fig. 19, which is a smooth spline approximated curve from measurements. It is important to notice the need for a correct approximation, in order to obtain a strictly monotone magnetization curve, as described in [40].

For the excitation, an impressed current in the coil, with a frequency of 5 kHz and a current of 5 kA is chosen. The material parameters of steel, together with the excitation frequency result in an approximate skin penetration depth of

$$\delta = \frac{1}{\sqrt{\pi f \gamma \mu}} = 0.702 \text{mm}. \tag{52}$$

To resolve the eddy currents properly, we discretize the skin depth with around five hexahedral elements, leading to an element size of $h = 0.14$ mm in the sheet. The discretization of air can be performed with large, unstructred tetrahedra, due to the non-conforming discretization approach. The volumes to be meshed are displayed in Fig. 20 and a crinkle clip of the mesh is shown in Fig. 21.
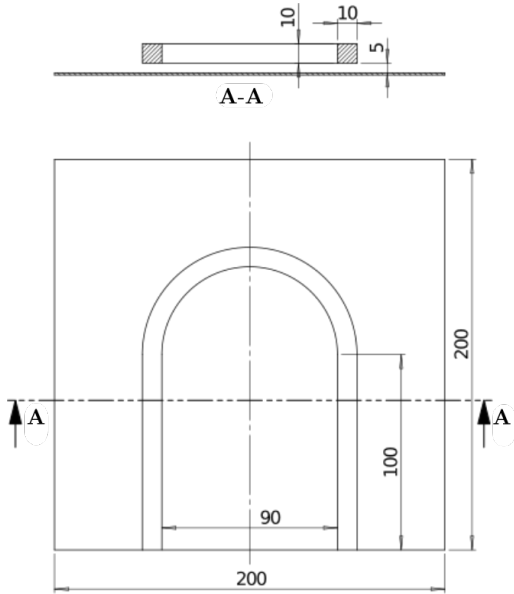
Fig. 18: Induction coil for heating a thin metal sheet (all dimensions in mm).
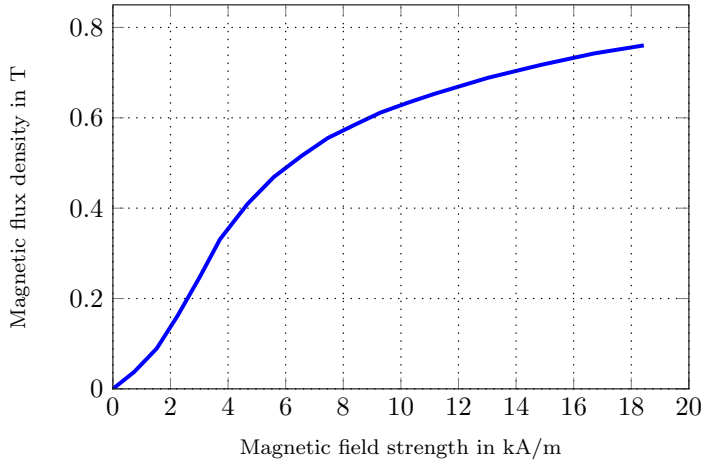
Fig. 19: Smooth spline approximated commutation curve from measurement.

This practical application demonstrates the enormous potential, because meshing in a conforming way draws high attention to element distortions when changing from fine to coarser grids, which is a tedious task. Furthermore, for the discretization of the sheet-air interface in a non-conforming way, shown in Fig. 22, one would need pyramid elements for the transition from hexahedra to tetrahedra.

With the non-conforming approach, the whole model consits just of 73550 elements, which results in approximately 79000 unknowns, when performing a transient analysis. For the multi-harmonic analysis, this number increases according to the coupling between the harmonics (see (36)).

For comparison of the nonlinear transient and the multi-harmonic results, we use a monitoring point on the surface of the sheet, right beneath the bending of the inductor. The nonlinear transient simulation was carried out for six periods, until a quasi steady state was reached
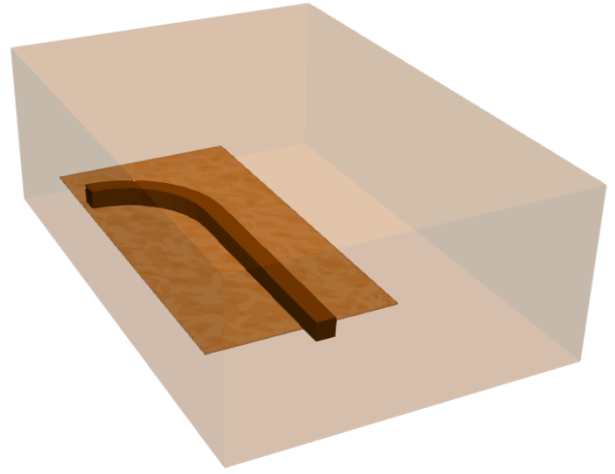
Fig. 20: Sheet with inductor and surrounding air volume.
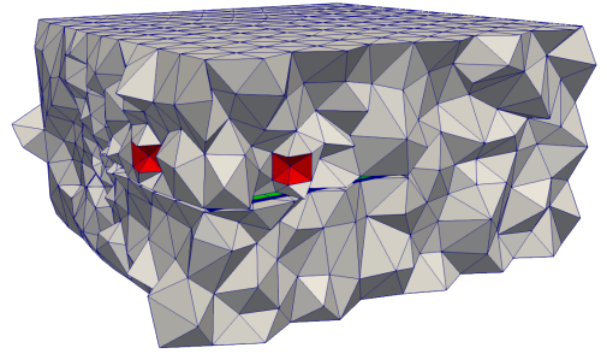
Fig. 21: Crinkle clip through the volume elements with the thin sheet in the middle part (green) and coil (red).

and the magnetic flux density result for one period is depicted in Fig. 23. In addition, the multi-harmonic results for different number of considered harmonics N are shown.

For induction heating processes, the more important quantity are the Joule and eddy current losses (51) and (47). In order to compare the nonlinear transient result for Joule losses, depicted in Fig. 24, with the multi-harmonic version, we numerically integrate the time-result over one period and divide by its period length. This procedure results in an averaged Joule loss density for the nonlinear transient simulation of $\hat{Q} = 3.6831 \cdot 10^7 \, \text{W/m}^3$. For the multi-harmonic simulations, the results and deviations from the nonlinear transient one are given in Tab. III.

We can clearly see the converging behavior, when considering more harmonics, on the relative error. At this point it should also be mentioned that the relative error strongly depends on the magnetization curve and therefore the material. When considering less steep BH-curves (smaller permeability) the errors decrease and therefore less harmonics need to be considered, which also decreases the numerical effort.

In Fig. 25 the global steady state temperature distribution is exemplarily given for the multi-harmonic analysis result with $N = 5$ and heat transport boundary conditions from sheet to air with a transport coefficient of $\alpha = 15 \, \text{W/(m}^2\text{K)}$ and ambient temperature of $10°C$.

Fig. 22: Cut through the volume elements, to see the nonconforming interface.
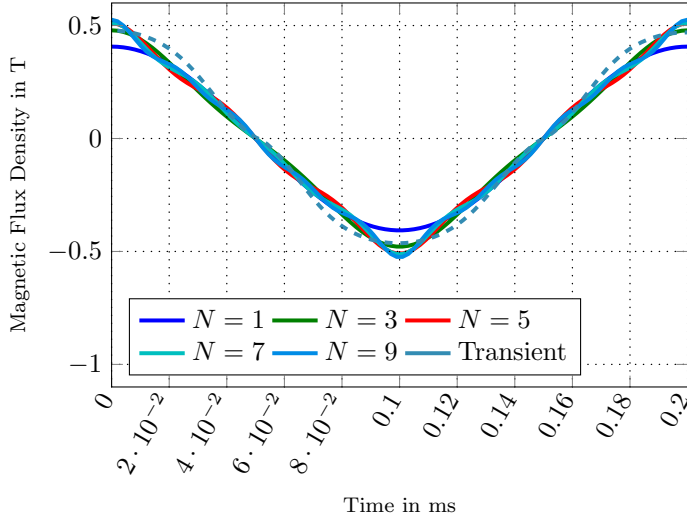
Fig. 23: Comparison of magnetic flux density from nonlinear transient and multi harmonic analysis for different number of harmonics N.

V. Conclusion

Non-conforming interfaces, both classical mortaring and Nitsche-type mortaring, drastically increase the performance of multiphysics simulations. Not only from the computational point of view, where we are striving for as few number of degrees of freedom as possible but also from a much more practical one, because having the flexibilty to mesh different regions completely independent of each other, is a huge benefit. To illustrate all these benefits, an induction heating process of a thin steel sheet was simulated. The region of interest, which is the steel sheet, is meshed with hexahedral elements including the

TABLE III: Comparison of multi-harmonic Joule losses with nonlinear transient ones.

N	Multi-harmonic $\tilde{Q}$	Relative Error
1	$3.24515 \cdot 10^7$	11.89%
3	$3.82366 \cdot 10^7$	3.82%
5	$3.79529 \cdot 10^7$	3.04%
7	$3.77344 \cdot 10^7$	2.45%
9	$3.75324 \cdot 10^7$	1.90%
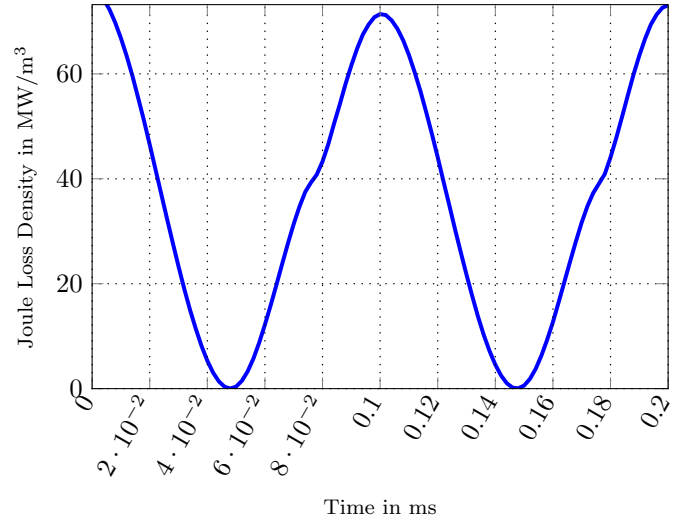
Fig. 24: Joule loss density of nonlinear transient simulation over one period of the base harmonic.

boundary layer for eddy currents, whereas the air volume is meshed by applying an unstructured tetrahedra-meshing algorithm. Another massive performance improvement, as long as we are only interested in the steady state solution of a certain physical field, is the presented harmonic balancing method using a multi-harmonic ansatz for all time periodic quantities. In our application, we could outperform the nonlinear transient simulation by a factor of 5 to 7, in terms of computational time.

References

[1] M. Kaltenbacher. Numerical Simulation of Mechatronic Sensors and Actuators: Finite Elements for Computational Multiphysics. *Springer, Berlin*, 3. Edition, 2015.

[2] U. Langer and P. Steinbach. Boundary element tearing and interconnecting methods. *Computing*, 71(3):205–228, 2003.

[3] N. Dokeva. Scalable Mortar Methods for Elliptic Problems on Many Subregions. *PhD Thesis, University of Southern California*, 2006.

[4] A. Toselli and O. B. Widlund. Domain decomposition methods - algorithms and theory. *Springer series in computational mathematics, Springer*, 2005.

[5] C. Farhat and M. Geradin. Using a reduced number of lagrange multipliers for assembling parallel incomplete field finite element approximations. *Computer Methods in Applied Mechanics and Engineering*, 97(3):333 – 354, 1992.

[6] B. Flemisch: Non-matching Triangulations of Curvilinear Interfaces Applied to Electro-Mechanics and Elasto-Acoustics. *PhD Thesis, University of Stuttgart*, 2006.

[7] C. R. Dohrmann, S. W. Key, and M. W. Heinstein. A method for connecting dissimilar finite element meshes in two dimensions. *International Journal for Numerical Methods in Engineering*, 48:655–678, 2000.

[8] C. Bernardi, N. Debit, and Y. Maday. Coupling of finite element and spectral element methods: first results. *Mathematics of Computation*, 54(21):21–39, 1990.

[9] D. Braess and W. Dahmen. Stability estimates of the mortar finite element method for 3-dimensional problems. *East-West Journal of Numerical Mathematics*, 6(4):249–263, 1998.

[10] F. B. Belgacem, P. Seshaiyer, and M. Suri. Optimal convergence rates of hp mortar finite element methods for second order elliptic problems. *M2AM Mathematical Modelling and Numerical Analysis*, 34(3):591–608, 2000.

[11] B. I. Wohlmuth. A mortar finite element method using dual spaces for the lagrange multiplier. *SIAM Journal on Numerical Analysis*, 38(3):989–1012, 2000.

[12] F. B. Benlacem, A. Buffa, Y. Maday. The mortar finite element method for 3D Maxwell equations: First results *SIAM Journal on Numerical Analysis*, 39(3):880–901, 2001
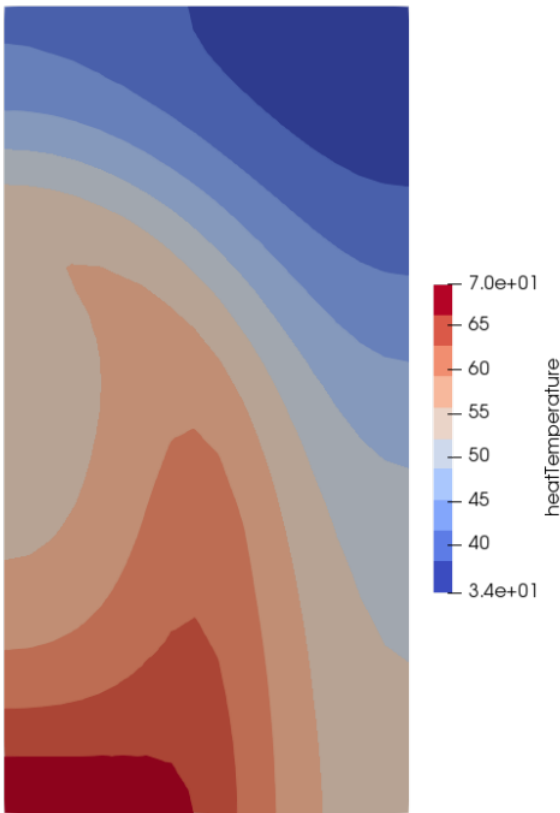
Fig. 25: Temperature distribution as obtained by the multi-harmonic simulation with 5 harmonics.

[13] R. W. H. Hoppe. Adaptive multigrid and domain decomposition methods in the computation of electromagnetic fields. *Journal of Computational and Applied Mathematics*, 168: 245–254, 2004

[14] S. Eiser. An Extension to Nitsche-type Mortaring for Non-conforming Finite Elements. *PhD Thesis, TU Wien*, 2016

[15] J. Nitsche: Über ein Variationsprinzip zur Lösung von Dirichlet-Problemen bei Verwendung von Teilräumen, die keinen Randbedingungen unterworfen sind. *Abhandlungen aus dem Mathematischen Seminar der Universität Hamburg*, 1971

[16] A. Hansbo, P. Hansbo, and M. G. Larson. A finite element method on composite grids based on nitsche's method. *ESAIM, Mathematical Modelling and Numerical Analysis*, 37(3):495–514, 2003.

[17] C. Annavarapu, M. Hautefeuille, and J. E. Dolbow. A robust Nitsch's formulation for interface problems. *Computer Methods in Applied Mechanics and Engineering*, 225-228: 44–54, 2012.

[18] B. Flemisch, M. Kaltenbacher, S. Triebenbacher, B. Wohlmuth. Non-Matching Grids for a Flexible Discretization in Computational Acoustics. *Communications in Computational Physics*, 11(2):472–488, 2012

[19] M. Kaltenbacher, S. Floss. Non-conforming Finite Elements Based on Nitsche-Type Mortaring for Inhomogeneous Wave Equation. *Journal of Theoretical and Computational Acoustics*, 2018

[20] H. Köck, S. Eisner, M. Kaltenbacher. Electrothermal multiscale modeling and simulation concepts for power electronics. *IEEE Transactions on Power Electronics*, 31(4), 3128–3140, 2016

[21] F. Toth, M. Kaltenbacher. Fully coupled linear modelling of incompressible free surface flow, compressible air and flexible structures. *International Journal for Numerical Methods in Engineering*, 107(11), 947–969, 2016

[22] M. Kaltenbacher, A. Hüppe, J. Grabinger, B. Wohlmuth. Modeling and Finite Element Formulation for Acoustic Problems Including Rotating Domains. *AIAA Journal*, 54(12), 3768–3777, 2016

[23] M. Kaltenbacher, A. Hüppe, A. Reppenhagen, F. Zenger, S. Becker. Computational Aeroacoustics for Rotating Systems with Application to an Axial Fan. *AIAA Journal*, 55(11), 3831–3838, 2017

[24] B. Flemisch, M. Kaltenbacher, B. I. Wohlmuth: Elasto-acoustic coupling on non-matching grids. *International Journal for Numerical Methods in Engineering*, 2006

[25] S. Triebenbacher: Nonmatching Grids for the Numerical Simulation of Problems from Aeroacoustics and Vibroacoustics. *PhD Thesis, Alps-Adriatic University of Klagenfurt*, 2012

[26] K. Hollaus, D. Feldengut, J. Schöberl, M. Wabro3, D. Omeragic. Nitsche-type Mortaring for Maxwell's Equations. *CiteSeer*, 2010

[27] Matuszyk, Pawel J. and Demkowicz, Leszek F. Parametric finite elements, exact sequences and perfectly matched layers. *Computational Mechanics*, 51: 35–45, 2013

[28] Zaglmayr S. High Order Finite Element Methods for Electromagnetic Field Computation. *PhD Thesis, Johannes Kepler University*, 2006

[29] Demkowicz, L. Computing with hp-aqdaptive finite elements: Volume one and two, dimensional elliptic and Maxwell problems. *CRC Press*, 2006

[30] Lo, D.S.H. Finite Element Mesh Generation. *Taylor & Francis*, 2015

[31] F. Bachinger and M. Kaltenbacher and S. Reitzinger An Efficient Solution Strategy for the HBFE Method. *10th IGTE Symposium*, 2002

[32] S. Reitzinger, J. Schöberl Algebraic multigrid for edge elements. *Numerical Linear Algebra with Applications*, 9: 223-238, 2002

[33] S. Reitzinger, M. Kaltenbacher Algebraic Multigrid Methods for Magnetostatic Field Problems. *IEEE Transactions on Magnetics*, 38(2): 477-480, 2002

[34] M. Hofer, M. Kaltenbacher, S. Reitzinger Algebraic Multigrid Preconditioner for Harmonic Eddy Current Problems in 3D. *IEEE Transactions on Magnetics*, 40(2): 1342-1345, 2004

[35] J. Driesen, G. Deliege T. Van Craenenbroeck, K. Hameyer. Implementation Of The Harmonic Balance FEM Method For Large-scale Saturated Electromagnetic Devices. *WIT Transactions on Engineering Sciences*, 1999

[36] J. Gyselinck, P. Dular, C. Geuzaine, W. Legros. Harmonic-balance finite-element modeling of electromagnetic devices: a novel approach. *IEEE Transactions on Magnetics*, 38(2):521-524, 2002

[37] O. Biro, G. Koczka, K. Preis. Finite element solution of nonlinear eddy current problems with periodic excitation and its industrial applications. *Applied Numerical Mathematics*, 79: 3–17, 2014

[38] Zeidler, E. and Boron, L.F. Nonlinear Functional Analysis and Its Applications: Part 2 B: Nonlinear Monotone Operators. *Springer*, 1989

[39] Bachinger F. Multigrid Solvers for 3D Multiharmonic Nonlinear Magnetic Field Computations. *PhD Thesis, Johannes Kepler University Linz*, 2003

[40] S. Reitzinger and B. Kaltenbacher and M. Kaltenbacher A note on the approximation of *BH*-curves for nonlinear magnetic field computations. *Technical Report, SFB F013: Numerical and Symbolic Scientific Computing*, Linz, 2002

[41] G. Ciarlet The Finite Element Method for Elliptic Problems. *SIAM*, 2002

All authors are part of the Institute of Mechanics and Mechatronics, at TU Wien, Austria

Klaus Roppert
klaus.roppert@tuwien.ac.at

Stefan Schoder
stefan.schoder@tuwien.ac.at

Florian Toth
florian.toth@tuwien.ac.at

Manfred Kaltenbacher
manfred.kaltenbachert@tuwien.ac.at